Coastal Dynamics 2017
Paper No. 012

DEPOSITION GRADIENTS ACROSS MANGROVE FRINGES

Erik M. Horstman[1], Julia C. Mullarney[1], Karin R. Bryan[1] and Dean R. Sandwell[1]

Abstract

Observations in a mangrove in the Whangapoua Harbour, New Zealand, have shown that deposition rates are greatest in the fringing zone between the tidal flats and the mangrove forest, where the vegetation is dominated by a cover of pneumatophores (i.e. pencil roots). Current speeds and suspended sediment concentrations dropped substantially across this zone. Near-bed turbulence within the fringe was substantially lower where the pneumatophore canopy was denser, facilitating the enhanced deposition in this zone. However, the near-bed conditions were not the primary control on the instantaneous sediment concentrations at this site. The total deposition across the different zones was the combined result of the reduced near-bed turbulence inside the vegetation and the larger-scale dynamics over the spatially variable vegetation cover, along with other confounding factors such as changing sediment inputs.

Key words: mangroves, vegetation gradients, turbulence, suspended sediment concentrations, sediment deposition

1. Introduction

Mangrove forests occur in intertidal areas at tropical and sub-tropical latitudes. Many of these forests are in low energy environments that are exposed to limited hydrodynamic forces. Mangroves have aerial roots that allow for root respiration above the water-logged soils (Tomlinson, 1986), and enable the trees to cope with the regular flooding of their environment by saline water. The shape of these aerial roots varies depending on the mangrove species, with the common root types being stilt roots, pneumatophores (pencil roots), knee roots and plank roots (Tomlinson, 1986). During high tides, these root systems are submerged, and together with the lower parts of the tree's stem and canopy, they impose a significant drag on ambient water movements. Consequently, mangroves have been observed to be effective attenuators of tidal currents (Horstman et al., 2013; Kobashi and Mazda, 2005), wind waves (Horstman et al., 2014; Mazda et al., 2006; Quartel et al., 2007) and even of longer wavelength tsunami waves (Danielsen et al., 2005; Kathiresan and Rajendran, 2005), provided the forest is of sufficient width (Mullarney and Henderson, 2017).

Together with the attenuation of currents and waves, mangroves reduce coastal erosion and facilitate sediment deposition (Furukawa and Wolanski, 1996; van Maanen et al., 2015; Van Santen et al., 2007). These biophysical interactions provide mangroves with a natural resilience which enables them to recover from erosion events as well as to combat land subsidence and relative sea level rise through enhanced sediment trapping (Gedan et al., 2011; Krauss et al., 2014; Stagg et al., 2016), provided an adequate sediment supply exists (Horstman et al., 2015; Willemsen et al., 2016). Consequently, mangroves are one of the intertidal ecosystems that have recently attracted attention for their ecosystem engineering capacities, offering a 'soft solution' to the multi-faceted challenges coastal communities are facing due to global (climate) change (Barbier et al., 2008; Bouma et al., 2014; Gedan et al., 2011; Temmerman et al., 2013).

The sediment trapping capacity of mangroves is key to their long-term resilience and the coastal protection they can provide. However, actual deposition rates are highly dependent on vegetation properties and geomorphological settings of the mangroves. In fact, while Young & Harvey (1996) observed a positive correlation between accretion rates and root densities in mangroves, erosion has also been observed in mangroves with relatively high root densities (Krauss et al., 2003; Spenceley, 1977). This

[1] Coastal Marine Group, Faculty of Science and Engineering, The University of Waikato, Private Bag 3105, Hamilton 3240, New Zealand. erik.horstman@waikato.ac.nz; julia.mullarney@waikato.ac.nz; karin.bryan@waikato.ac.nz; dean.sandwell@waikato.ac.nz

contrast in accretionary trends in mangroves depends on the balance between energy dissipation due to enhanced drag forces and the turbulence generation around these root systems (Norris et al., 2017).

While the enhanced drag in aquatic vegetation tends to diminish horizontal current velocities within the vegetation canopies, currents above and/or around the vegetation accelerate, causing velocity gradients over the canopy margins (Dunn et al., 1996; Nepf, 2012b; Yager and Schmeeckle, 2013). In the case of sufficiently dense canopies, shear over the canopy edges can give rise to canopy-scale turbulent motions (Ghisalberti and Nepf, 2005; Zong and Nepf, 2010). The penetration of these canopy-scale eddies into the vegetation canopy is reduced for greater vegetation densities. In addition to the canopy-scale turbulence, stem-scale turbulent motions are generated in the wakes of individual canopy elements, adding to the within-canopy turbulence (Mullarney and Henderson, 2017; Nepf, 2012a). Whereas increasing vegetation densities enhance the production of stem-scale turbulence, the concurrent reduction of the within-canopy flow velocity in denser canopies eventually causes the turbulence production to decrease (Nepf, 1999).

Elevated turbulence levels at the edges of vegetation canopies play a role in entraining sediments and sustaining enhanced suspended sediment concentrations (Tinoco and Coco, 2014). Once sediments are transported into the less dynamic zone within the vegetation canopy, sediment settling occurs. Both in an artificial salt marsh canopy on an intertidal flat and in an artificial eelgrass canopy in a flume, these processes were found to create scour zones before or around the leading edges of a dense canopy and to enhance deposition further into the dense canopy (Bouma et al., 2007; Le Bouteiller and Venditti, 2015). The same experiments showed that lower plant densities reduced scour at the leading canopy edge, associated with reduced local turbulence levels, and a more uniform deposition pattern was observed throughout these low-density canopies, associated with enhanced through-canopy flows.

The present study compares synoptic field observations of sediment deposition and turbulence in canopies of mangrove pneumatophores in order to obtain a better understanding of the sediment dynamics in mangrove fringes. These pneumatophore canopies show resemblance with the rigid dowel canopies that have been widely studied (e.g. Dunn et al., 1996; Ghisalberti and Nepf, 2005). However, turbulence patterns in variable-height pneumatophore canopies are found to deviate substantially from those in idealized uniform-height dowel canopies (Horstman et al., *in prep.*). The aim of this work is: (1) to study concurrent turbulence patterns and suspended sediment concentrations in a mangrove fringe; and (2) to examine links between these turbulence patterns, larger-scale transport processes and sediment deposition rates across a mangrove fringe.

2. Methods

2.1. *Study site*

Mangroves in New Zealand are at the southern limit of their global distribution, which extends from about 31^{o}N in southern Japan to about 39^{o}S in southern Australia, due to their intolerance to frost (Tomlinson, 1986). However, New Zealand mangroves are rapidly expanding due to increased sedimentation in estuaries following agricultural development and urbanization (Lovelock et al., 2007; Swales et al., 2007). The prograding trend of the mangroves in New Zealand makes for a suitable environment to study sediment deposition in mangrove ecosystems.

This study focusses on a cross-shore transect through a prograding mangrove forest located in the Whangapoua Harbour (Figure 1: 36°44’S, 175°39’E). Aerial photographs from the site show that no mangroves were present along this transect in 1971, whereas there currently exists a 300 m wide fringe of mangroves in front of a low stop bank on the southern edge of the Matarangi land spit (Figure 1.c).

Mangroves in New Zealand are mono-specific, consisting of relatively small *Avicennia marina* trees. The field site shows a characteristic zonation comprising an intertidal flat that is fronting a fringing region dominated by a ‘carpet’ of aerial roots that in turn precedes the denser mangrove forest, similar to many mangrove forests encroaching low-gradient tidal flats (e.g. Horstman et al., 2013; Norris et al., 2017). The intertidal flats in this area are locally covered with patches of seagrass (*Zostera muelleri*), showing up as dark patches in Figure 1.c. In the fringing region, the trees are sparser than in the forest and relatively small, yet there is a dense cover of pneumatophores (pencil roots) protruding from the bed. The forest has an open canopy consisting of trees ranging between about 1 and 3 m of height. The majority of the trees are

shrub-like with heights of less than 1.5 m, but these are interspersed with taller individuals that probably established at an earlier stage.

Figure 1. (a) Location of the study site within New Zealand, (b) overview of the Whangapoua Harbour and the Matarangi land spit, and (c) close-up of the transect across the mangrove fringe just south of Matarangi. The experimental transect is indicated with a white line (map data: Google, DigitalGlobe).

The study site is exposed to semi-diurnal tides with a maximum spring tide of 1.2 m above mean sea level (MSL) and a maximum spring tidal range of 2.5 m (NIWA, 2017). The elevation of the transect gradually increases from just above MSL at the start of the tidal flat, up to the maximum high water spring mark at the stop bank behind the forest. The mangrove fringe is located at an elevation of about 0.5 m above MSL.

2.2. *Data collection*

A suite of instruments was deployed at the field site from 11-19 April 2016, with some extended deployments lasting until 4 May 2016. Instruments were placed at nine stations along the transect, covering the three characteristic zones as outlined above as well as the channel that dissects the tidal flat (Figure 2).

For high-resolution velocity and turbulence measurements, an array of three vertically-separated Nortek Vectrino Profilers was used (Figure 3.a), each producing a vertical velocity profile of 30 cells of 1 mm, with a sampling rate of 50 Hz (cf. Mullarney et al., 2017). These Vectrino arrays were deployed for one tidal cycle at a single location and were then relocated over low tide. All deployments of the vertical Vectrino array concentrated on the fringing region around station 5 (Figure 2), to examine the hydrodynamics over the variable density of the pneumatophore cover. To monitor the larger-scale tidal currents across the fringe, upward looking Nortek Aquadopp Current Profilers were mounted on the bed at stations 3 and 7 and an upward looking Nortek Vector Current Meter was deployed at station 2 (Figure 2). The Aquadopps were programmed in high-resolution mode, providing a vertical profile consisting of 18 cells of 25 mm, ranging from approximately 18-63 cm above the bed, with a sampling rate of 8 Hz. The Vector recorded single point velocities at approximately 37 cm above the bed at 16 Hz.

Suspended sediment concentrations were monitored with independently logging Campbell Scientific OBS-3 sensors at stations 2 and 7 and with a Turner Scufa turbidity meter at station 3, at 37 cm, 34 cm and 34 cm above the bed, respectively. Time-averaged turbidity readings were stored every 5 or 10 minutes. Additionally, a vertical array of three Seapoint turbidity meters (connected to two RBR Concertos) was deployed at station 5 to continuously measure turbidity with a sampling rate of 2 Hz. The heights of this vertical array were similar to the heights of the Vectrino profiles, providing concurrent high-resolution vertical profiles of both the hydrodynamics and suspended sediment concentrations in the mangrove fringe.

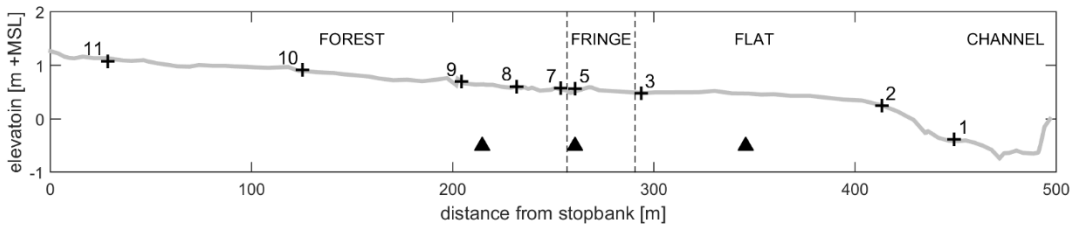

Figure 2. Cross-section of the study site in the Whangapoua Harbour. Instrument stations are marked with + and locations of sediment traps are indicated with ▲.

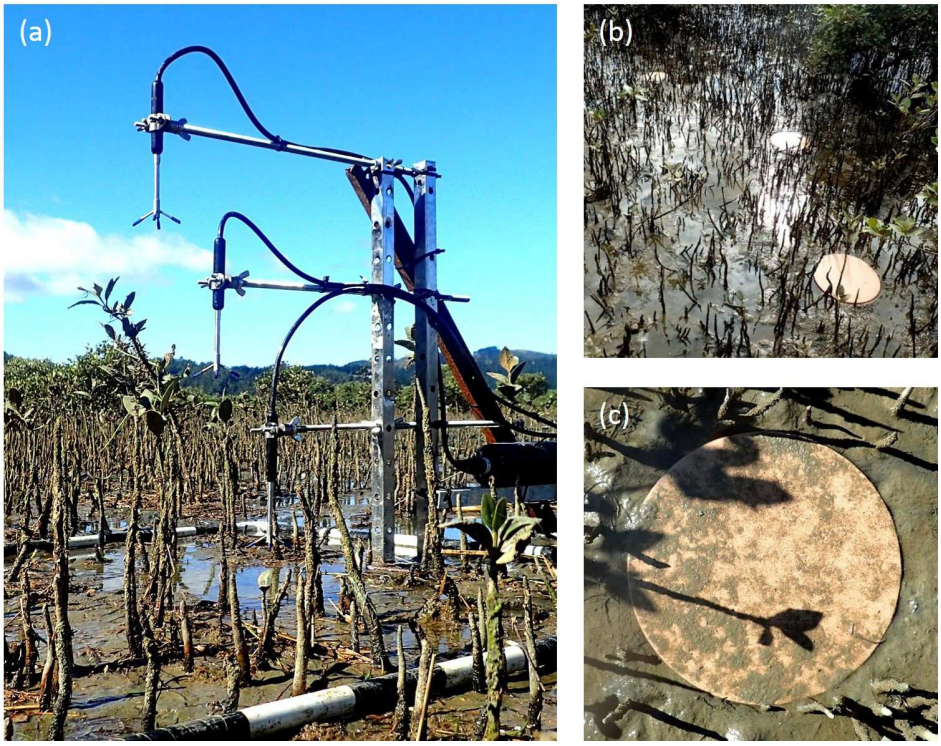

Figure 3. Field instrumentation in the mangrove fringe (around station 5 in Figure 2): (a) three vertically stacked Vectrino Profilers measuring flow patterns within, at the top of and above the pneumatophore canopy, (b) a set of three sediment traps that have just been deployed on 11 April 2016 and (c) one of these sediment traps upon collection on 15 April 2016, after 7 M2 tidal cycles.

Sediment deposition was monitored with sediment traps that were deployed for periods of a couple of days at a time. Sediment traps consisted of smooth terracotta discs with a 33 cm diameter that were leveled with the bed to induce minimal disturbance to the flow (Figure 3.b-c). The bottom sides of the discs were covered with tape to allow for easy cleaning upon retrieval. Sets of three traps each were deployed on the flat, in the fringe and in the forest (locations indicated in Figure 2).

In addition to these instrument deployments, an RTK GPS (Trimble) was used to survey the elevation profile along the transect. Local geodetic marks (Land Information New Zealand) were used to obtain an accurate vertical datum for this survey. Additionally, vegetation densities were quantified along the transect and at the vertical arrays of the Vectrino Profilers. For the vegetation densities along the transect, numbers (N), heights (h) and diameters (d) of the trees were surveyed in plots of 10x10 m^2 and the same was done for the pneumatophores in 5 subplots of 1x1 m^2 within each main plot. Vegetation surveys at the vertical Vectrino arrays comprised pneumatophore measurements in a 1x1 m^2 plot centered around the array. These data allowed for the computation of cross-sectional vegetation densities ($\varphi = N\pi d^2/4$).

2.3. *Data processing*

The data obtained with the Vectrino profilers required intensive pre-processing: first, data were transformed according to an improved calibration matrix obtained from Nortek after completion of the field experiments; second, the transformed data were filtered to remove correlations ≤70% and signal-to-noise ratios ≤15 dB (cf. Rusello et al., 2006); and third, the Doppler noise removal procedure of Hurther & Lemmin (2001) was applied to correct for the noise in the turbulent velocities by compensating for the covariance between the two vertical velocity signals that are obtained by the Vectrino. Subsequently, time-averaged ($\overline{u}$, $\overline{v}$, $\overline{w}$) and turbulent (u', v', w') velocity profiles were resolved, with *u*, *v* and *w* denoting observed velocity components in eastward, northward and upward (ENU) directions, respectively. Total horizontal velocities $U=(\overline{u}^2+\overline{v}^2)^{1/2}$ and turbulent kinetic energy $k=1/2\left(u'^2+v'^2+w'^2\right)$ were then computed for every data record. Regardless of the rigorous pre-processing, however, these velocity and turbulence profiles showed excessive variability along the vertical and hence this paper only presents the most reliable observations in the 'sweet spot' located at 50 mm below each probe (Nortek, 2011).

Data obtained with the Aquadopps were filtered to remove low signal strengths (<125 counts). Filtered data were averaged over bursts of 8.5 minutes (4096 samples) to compute time-averaged velocity profiles. Total horizontal velocities were then computed for every data record (as above) and depth-integrated over the observed velocity profiles. Data obtained with the Vectors were filtered to remove low-quality data with correlations ≤70% (cf. Rusello et al., 2006) and were rotated to earth coordinates (ENU) as well. Subsequently, the same parameters as above were calculated over blocks of 8.5 minutes (8192 samples).

The turbidity sensors recorded suspended sediment concentrations in NTU (Scufa, Seapoint) or a proxy thereof in milliVolts (OBS). These sensors were calibrated in a salt-water tank in the lab using sediment obtained from the field site. Water samples collected at each concentration increment were filtered (Whatman GF/C filters) and oven dried (24 hrs at 105°C) to compute the suspended sediment concentrations in the tank. Linear fits to the obtained data produced highly significant calibration curves (r^2=1.00) that were then applied to compute suspended sediment concentrations from the output of the turbidity sensors. Additionally, the 2 Hz output of the Seapoint turbidity meters was averaged over 2.5 minute intervals and, lastly, outputs of all turbidity meters were filtered to remove data when the sensors were emerged and to remove artificial spikes that were produced upon submergence and emergence of the sensors.

Trapped sediments were processed to obtain the total dry mass of the yields per trap. The bulk of the sediments on the traps was scraped off and processed directly, after which the remainder of the deposits was washed off the traps and filtered (Whatman GF/C filters). The total yields of the traps were then oven dried (at 105°C) until a constant dry weight was obtained.

3. Results

3.1 *Turbulence in mangrove pneumatophores*

Vertical profiles of the hydrodynamics within the mangrove fringe were collected with the vertical array of Vectrino Profilers at locations with sparse and dense pneumatophore covers. Pneumatophore densities within the 1 m^2 area surrounding the Vectrino arrays were 84 and 219 m^{-2}, respectively, resulting in canopy densities presented in Table 1. The average heights of the pneumatophores in these plots increased with density and were about 7 and 12 cm, respectively. Additionally, the plot with the sparse pneumatophore cover included some patches of seagrass of about 5 cm length, which were also found on the tidal flat. The density of the dense pneumatophores at the fringe was similar to the vegetation density inside the forest.

The velocities obtained in the densely and sparsely vegetated parts of the fringe differed substantially (Table 1). Both within and above the sparser canopy, tidal currents were found to be stronger than at the denser pneumatophore canopy, with maximum flow speeds that were up to 35% higher at about 0.4 m above the bed and 108% higher near the bed within the sparse canopy (Figure 4.a-b). Consequently, maximum depth-averaged (over the three observation points) velocities were 8.7 cm/s for the sparse canopy and only 5.8 cm/s for the dense canopy.

At the dense canopy site, highest turbulence was observed at 0.4 m above the bed, while turbulence was very low within the pneumatophores (Figure 4.c). Conversely, for the sparse canopy, turbulence was lowest

at 0.4 m above the bed and substantially higher near the bed within the pneumatophores (Figure 4.d). The maximum turbulence inside the sparse canopy was 3.5 times greater than in the dense pneumatophores, whereas turbulence at 0.4 m height was 6 times lower over the sparse canopy than over the dense canopy.

Table 1. Biophysical parameters for the flat, fringe and forest zone of the study site.

	φ [-]	$U_{max,flood}$ [m/s]	$U_{max,ebb}$ [m/s]	k_{max} [m^2/s^2]	$k_{max,bed}$ [m^2/s^2]
Flat	0	0.22	0.20	-	-
Fringe - sparse	0.0032	0.14	0.14	$3.4 \cdot 10^{-4}$	$2.2 \cdot 10^{-4}$
Fringe - dense	0.0084	0.10	0.08	$7.0 \cdot 10^{-4}$	$6.2 \cdot 10^{-5}$
Forest	0.0081	0.05	0.05	-	-

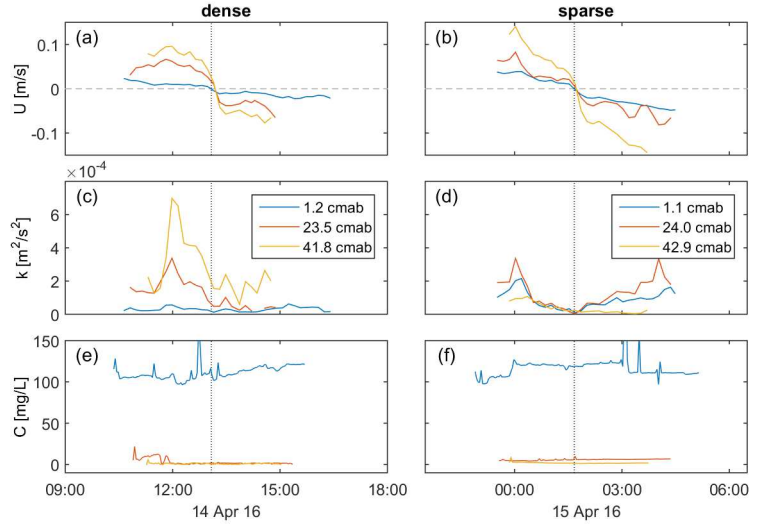

Figure 4. Synoptic overview of vertical variations of (a,b) tidal currents, (c,d) turbulent kinetic energy and (e,f) suspended sediment concentrations at two locations in the fringe with a dense and sparse pneumatophore density, respectively (cmab = cm above bed). Suspended sediment concentrations were all obtained in the dense canopy, at heights coincident with the hydrodynamic data (at 2, 25 and 43 cmab, respectively). Vertical dotted lines mark the occurrence of high tide.

At both locations, a turbulence peak was observed to coincide with the maximum flow speeds on the incoming tide. Above the dense canopy, turbulence mainly declined after this peak had occurred and there was only a minor increase of the near-bed turbulence at the final stages of ebb tide (Figure 4.c). Conversely, turbulence in the sparse canopy showed a distinct minimum on high slack tide and then increased again from the start of ebb tide towards a second maximum that was reached with the highest velocities during the ebb tidal stage (Figure 4.d).

Observed suspended sediment concentrations (C) above the pneumatophore canopy were low on both days, not exceeding 10 mg/L. Close to the bed, however, concentrations fluctuated between 100-125 mg/L (Figure 4.e-f). These observed near-bed sediment concentrations showed a gradual increase over time on 14 April (Figure 4.e), suggesting that sediment may have been settling from the upper parts of the water column while the turbulence reduces (Figure 4.c). However, the concentrations at the upper observation points and on 15 April did not show any major trends over time and were uncorrelated with the locally observed velocity and turbulence variations.

3.2 Variations of hydro- and sediment dynamics across the fringe

Simultaneously with the turbulence observations within the fringe, currents and suspended sediment were monitored along the entire transect as to provide information on the larger scale dynamics on the flats, at the fringe and inside the forest.

Currents at stations 2, 3 and 7 were consistently perpendicular to the transect, directed east-southeast

during flood tide and west-northwest during ebb tide. These directions are roughly parallel to the main direction of the channel fronting the tidal flat and also coincide with the orientation of the sub-estuary wherein the study site is located (Figure 1.c). Figure 5.a-c present time series of the time-averaged total horizontal velocities *U*, showing a clear deceleration of the currents along the transect. Across the tidal flat, between stations 2 and 3, observed maximum currents during the flood stage reduced by 30-45% over a distance of 120 m. Across the fringe zone, between stations 3 and 7 which are only 40 m apart, maximum currents during the flood stage reduced by 65-75%. During the ebb stage, currents through the fringe and over the flat were slightly weaker than during the flood stage over the first two days, by up to 25%. This inequality between the maximum velocities on both tidal stages was not observed anymore inside the forest (Figure 5.a-b). On 19 April, when the high tide was 15-20 cm lower than on the 14th and 15th, maximum current velocities were similar on both tidal stages at all the three locations (Figure 5.c).

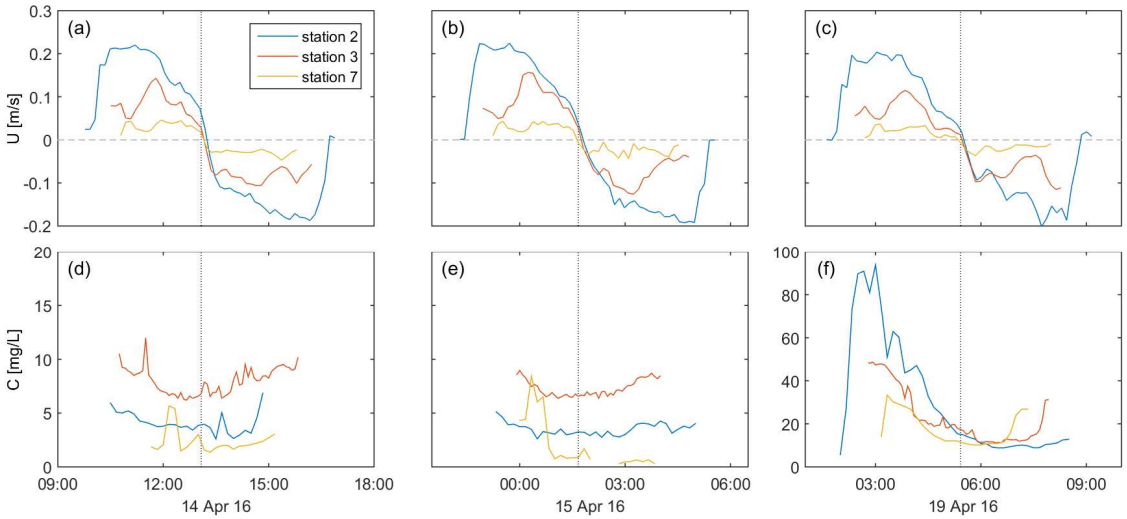

Figure 5. Time-series of (a-c) current velocities and (d-f) concurrent suspended sediment concentrations at three positions along the transect during three different M2 tidal cycles on 14, 15 and 19 April 2016, respectively. Vertical dotted lines mark the occurrence of high tide (at station 3, for station locations see Figure 2).

Typically, currents at the front of the flat (station 2) peaked at the start of the flood tide and at the end of the ebb tide. This pattern was found to change in front of the mangrove fringe (station 3), where velocities peaked around mid-tide during both the flood and the ebb stages. The pneumatophore vegetation at the fringe (for densities see Table 1) added a near-bed drag component that limited the flow speeds at lower water depths in this area, causing the velocities of the currents at both tidal stages to peak at higher water depths. Inside the forest (station 7), where the vegetation density was greatest, no pronounced peak of the flow speeds was observed.

Suspended sediment concentrations were low and generally did not exceed 10 mg/L (Figure 5.d-e). Sediment concentrations were monitored at similar heights above the bed (~1-2 cm different) and so spatial differences in sediment concentrations could be interpreted to provide insight into cross-shore transport processes. The observed suspended sediment concentrations generally had a maximum value upon or shortly after submergence and showed a slight decrease during flood tide, even while the currents were increasing towards maximum flood. Conversely, after high slack tide the concentrations gradually increased again as with the increasing flow speeds on the ebb tidal stage, with the increase persisting after maximum current velocities had been reached. The observed increase of the concentrations between stations 2 and 3 suggests the currents entrain sediments from the (partly bare) flats in front of the mangroves. Conversely, sediment concentrations declined between the start of the fringe (station 3) and the interior of the forest (station 7), indicating (enhanced) deposition in these zones.

Suspended sediment concentrations were an order of magnitude greater on 19 April (Figure 5.f) compared to the previous two days. This was caused by a torrential rain storm on the 17th (114 mm of rainfall in 24 hours), which had released a large amount of debris and sediments from the catchment into the estuary. On the following days, high suspended sediment concentrations were observed on the initial

stages of flood tide all along the transect, with concentrations of up to 100 mg/L just beside the channel, which rapidly declined during high tide and remained constant around 10-15 mg/L during the subsequent ebb tide. These sediment concentrations showed a substantial drop between stations 2 and 3, indicating that the suspended sediments were largely deposited on the flat. The greater sediment concentrations at stations 3 and 7 still showed a cross-shore decrease over the fringe during most of the tide, apart from the final stages of ebb, corroborating sustained deposition in this zone.

3.3 *Sediment deposition rates*

Sediment trap yields were analyzed for two subsequent time intervals: 11-15 April and 17-19 April, covering 7 and 4 M2 tidal cycles, respectively. Both datasets clearly show enhanced trapping of sediments in the forest's fringe. Sediment accretion, standardized to a deposition rate per tide, was 2.5-3 times greater in the fringe than on the adjoining tidal flats or within the forest (Figure 6). Sediment traps in the fringe were located in the area of dense pneumatophores (see Figure 3), where near bed turbulence is small, consistent with the results shown in Figure 4. Due to the increased sediment load of the water at all stations after the rain storm (Figure 5.f) and facilitated by reduced tidal currents due to neap tidal conditions (Figure 5.c), deposition rates doubled throughout all three zones in this period.

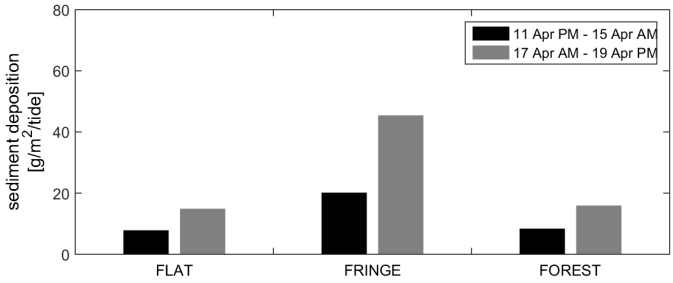

Figure 6. Deposition rates for each of the three zones along the transect (see Figure 2 for locations). Results cover two subsequent measurement periods and are standardized to deposition rates per tide.

4. Discussion

Observed turbulence profiles in the mangrove fringe provide a first impression of the impacts of vegetation density on the vertical distribution of turbulent energy and can be inferred on the cross-shore dynamics over a mangrove fringe with gradually increasing vegetation densities. The pneumatophore cover in the fringe generally increased from sparse at the front of the fringe to a dense cover at the interface with the forest, forming a gradual transition from the bare tidal flat to the densely vegetated forest zone (Table 1).

The higher near-bed velocity and turbulence in the sparse canopy, compared to the dense canopy (Figure 7), allowed for greater bed shear stresses than the dense canopy, as has been observed before in flume experiments with flexible vegetation mimics on a fine sand bed (Le Bouteiller and Venditti, 2015). Inferring this trend to the bare tidal flat suggests even greater near-bed velocities, in line with generally observed log-normal velocity profiles over bare beds, and consequently higher bed shear stresses (e.g. Bouma et al., 2007). The reduction of the bed shear in the pneumatophore fringe allowed for enhanced sediment settling and hence deposition rates in the fringe were generally substantially higher than on the tidal flat (Figure 6).

The limited deposition on the tidal flat is corroborated by the observed sediment concentrations that were initially found to increase in the landward direction (Figure 5.d-e), which could indicate re-entrainment of sediments. However, the increase in suspended sediment concentrations after a rain storm reversed this trend into a general decline of the concentration over the flat (Figure 5.f). This event coincided with a period of reduced (neap) tidal dynamics (Figure 5.c) that may have caused the turbulence levels and bed shear on the flats and in the fringe to drop, potentially explaining why the re-entrainment observed in the earlier two days did not occur on the last observation day (Figure 5.f).

Enhanced turbulence above the (denser) pneumatophore canopies in the fringe has the potential to carry

greater suspended sediment concentrations (Tinoco and Coco, 2016; Yang et al., 2016). Regardless, sediment concentrations in the forest were generally substantially lower than those just in front of the fringe (Figure 5.d-f) and hence deposition rates in the forest remained lower than those within the fringe (Figure 6). This pattern follows general deposition patterns across vegetation fringes, showing a general decline of the deposition rate with distance into the vegetation (Bouma et al., 2007; Le Bouteiller and Venditti, 2015; Van Santen et al., 2007).

Spatial variability of sediment accretion rates within the fringe have not been addressed in this study, but are likely to exist due to the observed variations in current velocities and turbulence production in variable density pneumatophore canopies (cf. Norris et al., 2017). The effect of the varying pneumatophore density on turbulence matched the findings from more controllable lab experiments on the hydrodynamic properties of flows within and above pneumatophore canopies (Horstman et al., *in prep.*). These experiments were run for real pneumatophores at vegetation densities of φ = 0.0023, 0.0049 and 0.0086.

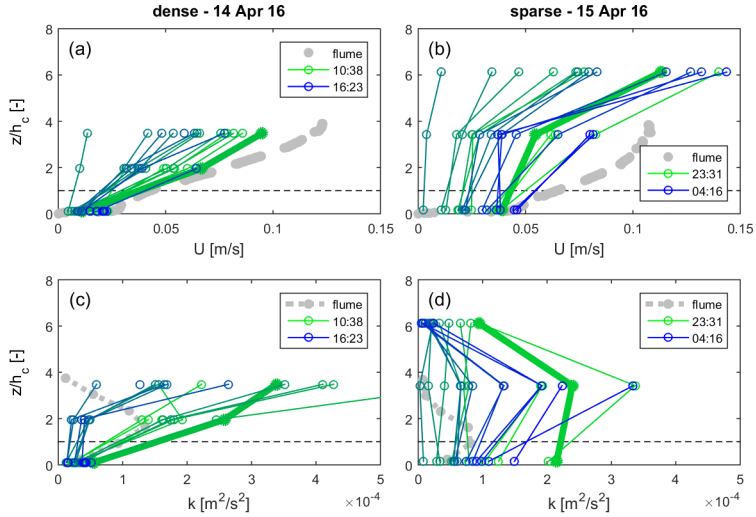

Figure 7. Comparison of (a,b) observed velocity and (c,d) turbulence profiles in the field with data from an experimental study with real pneumatophores in a flume. Field observations show quarter-hourly vertical profiles of the data presented in Figure 4, shaded from green (flood) to blue (ebb). Flume data were obtained for pneumatophore densities φ = 0.0086 (a,c) and 0.0023 (b,d) and a free-stream velocity (without pneumatophores) of 0.10 m/s. The elevation on the vertical axis is standardized by the average canopy height of the pneumatophores h_c. The thicker printed profiles are those for which the highest observed velocity is closest to the free-stream velocity in the flume.

The field data were compared to a set of experiments with a 30 cm water depth and with a constant flow forcing causing a free-stream velocity of 0.10 m/s prior to introduction of the pneumatophores (Figure 7). For the dense pneumatophore canopy, the velocity profiles observed in the flume for a steady unidirectional current tend to form the envelope for the field observations in dynamic tidal currents (Figure 7.a). Compared to the regular log-normal velocity profile, flow within the canopy ($z/h_c < 1$) was reduced and above the canopy ($z/h_c > 1$) currents were enhanced, with near-bed velocities up to ten times lower than the above-canopy velocities (Figure 4.a). In the sparse pneumatophores in the field, near-bed velocities increased compared to those in the denser canopies, similar to the flume measurements (Figure 7.b). However, free-stream velocities at six times the canopy height of the sparse pneumatophores became greater than those in the flume. It is uncertain as to what extent the latter might have been caused by spatial variations in the free-stream velocity over the variable-density pneumatophore canopy in the field.

The shear over the top of a dense canopy can produce canopy-scale Kelvin Helmholtz vortices (Nepf, 2012a), which likely explains the peak in the turbulence profile just above the canopy in the flume experiments (Figure 7.c-d). Because the shear over the dense pneumatophore canopy in the field was substantial (Figure 7.a), there was a great potential for the generation of canopy-scale turbulence just above the dense canopy. Meanwhile, turbulence was very low within the dense pneumatophores, a possible consequence of the reduced penetration of canopy-scale turbulence into the canopy and the reduced generation of stem-scale turbulence due to the lower flow speeds within the dense canopy (Nepf, 2012a).

For the sparse canopy, near-bed velocities were only about four times smaller than the above-canopy velocities (Figure 7.b), limiting the vertical shear and hence the generation of canopy-scale turbulence, while the higher within-canopy velocities and the greater spacing of the pneumatophores could enhance within-canopy turbulence (Figure 7.d). The maximum turbulence inside the dense canopy was 3.5 times lower than in the sparse pneumatophores, whereas turbulence at 0.4 m height was more than six times greater over the dense canopy than over the sparse canopy (Figure 4.c,d).

Turbulence levels in the field were much higher than in the flume, especially at greater elevations above the vegetation. For the sparse canopy, turbulence peaked at about 3.5 times the average pneumatophore height (Figure 7.d), but over the dense canopy turbulence was found to increase beyond the highest observation at four times the canopy height (Figure 7.c). The much greater increase of turbulence with the height above the bed in the field might be caused by the greater water depths compared to the flume, potentially allowing for larger-scale boundary-layer vortices to develop over the vegetation (Nepf, 2012a). Another contributing factor could be the presence of saplings and trees in the mangrove fringe (see Figure 3.a-b), enhancing turbulence production at greater heights above the bed.

Unlike the clear relations between pneumatophore densities and the near-bed turbulence, no correlations between the near-bed turbulence and suspended sediment concentrations could be derived from the present observations (Figure 4). Likewise, greater flow speeds did not necessarily coincide, in time or in place, with higher suspended sediment concentrations (Figure 5). Hence it was concluded that near-bed conditions were not the primary control on the instantaneous sediment concentrations at this site. Rather, confounding factors such as (episodic) inputs of sediments were found to have a major impact on sediment concentrations in the water, showing that sediments are likely advected into the study site.

5. Conclusions

Field observations of sediment deposition rates across a mangrove fringe showed the deposition in the fringing pneumatophore zone, the area that separates the tidal flats and the mangrove forest, to be greater than in the adjoining zones. The enhanced deposition in the pneumatophore fringe followed from a sharp decline in the suspended sediment concentrations across this zone, as the reduction of near-bed velocities and turbulence in the pneumatophores facilitated sediment settling and limited resuspension. Conversely, sediment concentrations were found to increase over the tidal flats in front of the pneumatophores, where the lack of vegetation allowed for greater near-bed dynamics that limited the deposition and might even have facilitated resuspension of sediments. Sediment concentrations within the forest were consistently low, thereby limiting the within-forest deposition rates.

Within the fringe, near-bed velocities and turbulence were found to be much greater in a sparse pneumatophore canopy than in a dense pneumatophore canopy. Conversely, the lower within-canopy velocities in the denser pneumatophores resulted in enhanced shear across the top of the canopy, creating stronger turbulence above the pneumatophores. Nevertheless, observed trends in turbulence profiles varied across the different tidal cycles that were studied and deviated from the turbulence profiles that were collected in a controlled flume experiment with real pneumatophores. Also, the turbulence profiles did not provide unequivocal relations with concurrently observed sediment concentrations in the water column. These relations must depend on a range of other confounding factors, such as larger scale transport processes and variable sediment inputs. Contributions to the deposition patterns across mangrove fringes by these other confounding factors will be addressed in future work.

Acknowledgements

This research is funded by the Royal Society of New Zealand’s Marsden Fund (14-UOW-011). Historic images of the field site were kindly provided by Mark Hall. We thank Ngati Hei and Ngati Huarere for their interest in and support of our work.

References

Barbier, E.B. et al., 2008. Coastal ecosystem-based management with nonlinear ecological functions and values. *Science*, 319(5861): 321-323.

Bouma, T.J. et al., 2014. Identifying knowledge gaps hampering application of intertidal habitats in coastal protection: Opportunities & steps to take. *Coastal Engineering*, 87: 147-157.

Bouma, T.J. et al., 2007. Spatial flow and sedimentation patterns within patches of epibenthic structures: Combining field, flume and modelling experiments. *Continental Shelf Research*, 27: 1020-1045.

Danielsen, F. et al., 2005. The Asian Tsunami: A protective role for coastal vegetation. *Science*, 310(5748): 643.

Dunn, C., Lopez, F. and Garcia, M., 1996. *Mean flow and turbulence in a laboratory channel with simulated vegetation*, University of Illinois.

Furukawa, K. and Wolanski, E., 1996. Sedimentation in Mangrove Forests. *Mangroves and Salt Marshes*, 1(1): 3-10.

Gedan, K.B., Kirwan, M.L., Wolanski, E., Barbier, E.B. and Silliman, B.R., 2011. The present and future role of coastal wetland vegetation in protecting shorelines: answering recent challenges to the paradigm. *Climatic Change*, 106(1): 7-29.

Ghisalberti, M. and Nepf, H., 2005. Mass transport in vegetated shear flows. *Environmental Fluid Mechanics*, 5(6): 527-551.

Horstman, E.M., Dohmen-Janssen, C.M., Bouma, T.J. and Hulscher, S.J.M.H., 2015. Tidal-scale flow routing and sedimentation in mangrove forests: Combining field data and numerical modelling. *Geomorphology*, 228: 244-262.

Horstman, E.M., Dohmen-Janssen, C.M. and Hulscher, S.J.M.H., 2013. Flow routing in mangrove forests: A field study in Trang province, Thailand. *Continental Shelf Research*, 71: 52-67.

Horstman, E.M. et al., 2014. Wave attenuation in mangroves: A quantitative approach to field observations. *Coastal Engineering*, 94: 47-62.

Horstman, E.M., Mullarney, J.C., Bryan, K.R., Pilditch, C.A. and Eager, C.A., *in prep.* Differences of hydrodynamics in real and artificial mangrove pneumatophores.

Hurther, D. and Lemmin, U., 2001. A Correction Method for Turbulence Measurements with a 3D Acoustic Doppler Velocity Profiler. *Journal of Atmospheric and Oceanic Technology*, 18(3): 446-458.

Kathiresan, K. and Rajendran, N., 2005. Coastal mangrove forests mitigated tsunami. *Estuarine, Coastal and Shelf Science*, 65(3): 601-606.

Kobashi, D. and Mazda, Y., 2005. Tidal flow in riverine-type mangroves. *Wetlands Ecology and Management*, 13(6): 615-619.

Krauss, K.W., Allen, J.A. and Cahoon, D.R., 2003. Differential rates of vertical accretion and elevation change among aerial root types in Micronesian mangrove forests. *Estuarine, Coastal and Shelf Science*, 56(2): 251-259.

Krauss, K.W. et al., 2014. How mangrove forests adjust to rising sea level. *New Phytologist*, 202(1): 19-34.

Le Bouteiller, C. and Venditti, J.G., 2015. Sediment transport and shear stress partitioning in a vegetated flow. *Water Resources Research*, 51(4): 2901-2922.

Lovelock, C.E. et al., 2007. Mangrove growth in New Zealand estuaries: the role of nutrient enrichment at sites with contrasting rates of sedimentation. *Oecologia*, 153(3): 633-641.

Mazda, Y., Magi, M., Ikeda, Y., Kurokawa, T. and Asano, T., 2006. Wave reduction in a mangrove forest dominated by *Sonneratia* sp. *Wetlands Ecology and Management*, 14(4): 365-378.

Mullarney, J.C. and Henderson, S.M., 2017. Flows within marine vegetation canopies. In: V. Pan-chang and J. Kaihatu (Editors), Advances in Coastal Hydraulics (in press). World Scientific Publishing Ltd.

Mullarney, J.C. et al., 2017. A question of scale: The role of turbulence within mangrove roots in shaping the Mekong Delta. *Oceanography (under review)*.

Nepf, H.M., 1999. Drag, turbulence, and diffusion in flow through emergent vegetation. *Water Resources Research*, 35(2): 479-489.

Nepf, H.M., 2012a. Flow and Transport in Regions with Aquatic Vegetation. *Annual Review of Fluid Mechanics*, 44(1): 123-142.

Nepf, H.M., 2012b. Hydrodynamics of vegetated channels. *Journal of Hydraulic Research*, 50(3): 262-279.

NIWA, 2017. *Tide forecaster*, https://www.niwa.co.nz/services/online-services/tide-forecaster.

Norris, B.K., Mullarney, J.C., Bryan, K.R. and Henderson, S.M., 2017. The effect of pneumatophore density on turbulence: a field study in a Sonneratia-dominated mangrove forest, Vietnam. *Continental Shelf Research (under review)*.

Nortek, 2011. *Vectrino-II profiling velocimeter User Guide*.

Quartel, S., Kroon, A., Augustinus, P.G.E.F., Van Santen, P. and Tri, N.H., 2007. Wave attenuation in coastal mangroves in the Red River Delta, Vietnam. *Journal of Asian Earth Sciences*, 29(4): 576-584.

Rusello, P.J., Lohrmann, A., Siegel, E. and Maddux, T., 2006. Improvements in acoustic doppler velocimetery. *The 7th Int. Conf. on Hydroscience and Engineering*: 1-16.

Spenceley, A.P., 1977. The role of pneumatophores in sedimentary processes. *Marine Geology*, 24(2): M31-M37.

Stagg, C.L. et al., 2016. Processes Contributing to Resilience of Coastal Wetlands to Sea-Level Rise. *Ecosystems*, 19(8): 1445-1459.

Swales, A., Bentley, S., Lovelock, C. and Bell, R., 2007. Sediment processes and mangrove-habitat expansion on a rapidly-prograding muddy coast, New Zealand, Coastal Sediments '07. American Society of Civil Engineers: 1441-1454.

Temmerman, S. et al., 2013. Ecosystem-based coastal defence in the face of global change. *Nature*, 504(7478): 79-83.
Tinoco, R.O. and Coco, G., 2014. Observations of the effect of emergent vegetation on sediment resuspension under unidirectional currents and waves. *Earth Surf. Dynam.*, 2(1): 83-96.
Tinoco, R.O. and Coco, G., 2016. A laboratory study on sediment resuspension within arrays of rigid cylinders. *Advances in Water Resources*, 92: 1-9.
Tomlinson, P.B., 1986. *The botany of mangroves*. Cambridge tropical biology series. Cambridge University Press.
van Maanen, B., Coco, G. and Bryan, K.R., 2015. On the ecogeomorphological feedbacks that control tidal channel network evolution in a sandy mangrove setting. *Proceedings of the Royal Society of London A: Mathematical, Physical and Engineering Sciences*, 471(2180): 1-24.
Van Santen, P., Augustinus, P.G.E.F., Janssen-Stelder, B.M., Quartel, S. and Tri, N.H., 2007. Sedimentation in an estuarine mangrove system. *Journal of Asian Earth Sciences*, 29(4): 566-575.
Willemsen, P.W.J.M., Horstman, E.M., Borsje, B.W., Friess, D.A. and Dohmen-Janssen, C.M., 2016. Sensitivity of the sediment trapping capacity of an estuarine mangrove forest. *Geomorphology*, 273: 189-201.
Yager, E.M. and Schmeeckle, M.W., 2013. The influence of vegetation on turbulence and bed load transport. *Journal of Geophysical Research*, 118(3): 1585-1601.
Yang, J.Q., Chung, H. and Nepf, H.M., 2016. The onset of sediment transport in vegetated channels predicted by turbulent kinetic energy. *Geophysical Research Letters*, 43(21): 11,261-11,268.
Young, B.M. and Harvey, E.L., 1996. A Spatial Analysis of the Relationship Between Mangrove (Avicennia marina var. australasica) Physiognomy and Sediment Accretion in the Hauraki Plains, New Zealand. *Estuarine, Coastal and Shelf Science*, 42(2): 231-246.
Zong, L. and Nepf, H., 2010. Flow and deposition in and around a finite patch of vegetation. *Geomorphology*, 116(3–4): 363-372.